# Determination of the structural properties of a novel two-dimensional Prussian blue analogue by transmission electron microscopy

by

DANIEL SALVATORE BADALI

B.Sc. (Honours), University of Toronto, 2011

Dissertation submitted in partial fulfillment
of the requirements for the degree of
Masters of Science

Faculty of Mathematics, Informatics and Natural Sciences
Department of Physics
Universität Hamburg

March 2015
HAMBURG

Date of oral defense: March 16, 2015

The following reviewers recommend the admission of the dissertation:

Prof. R.J. Dwayne Miller

Max Planck Institute for the
Structure and Dynamics of Matter
CFEL (Bldg. 99), Room 2.099
Luruper Chausee 149
22761 Hamburg, Germany
Tel.: +49-(0)-40-8998-6200
Email: dwayne.miller@mpsd.mpg.de

Prof. Claudiu C. Gradinaru

University of Toronto Mississauga
Davis Building, Rm 5019
3359 Mississauga Road North
Mississauga, ON, Canada
L5L 1C6
Tel.: (905)-828-3833
Email: claudiu.gradinaru@utoronto.ca

Hiermit bestätige ich, dass die vorliegende Arbeit von mir selbständig verfasst wurde und ich keine anderen als die angegebenen Hilfsmittel  insbesondere keine im Quellenverzeichnis nicht benannten Internet-Quellen  benutzt habe und die Arbeit von mir vorher nicht einem anderen Prüfungsverfahren eingereicht wurde. Die eingereichte schriftliche Fassung entspricht der auf dem elektronischen Speichermedium. Ich bin damit einverstanden, dass die Bachelorarbeit veröffentlicht wird.

Toronto, den March 4, 2015 Daniel Salvatore Badali

# Summary

Two-dimensional materials have been at the forefront of materials science research in the past decade due to the fact that their physical properties are often vastly different from their bulk counterparts. This makes them an exciting venue to explore, and many monolayers and thin films have found uses as platforms for device applications. This work combines this two-dimensional world with another exciting field, functional coordination compounds, by synthesizing truly two-dimensional crystals of Prussian blue analogues (PBA). The synthesis was mediated by a novel variant of the Langmuir-Schaefer technique, which provides a two-dimensional surface on which the formative reaction can take place. Two-dimensionality was imposed by restricting the coordination level of one of the precursors. By using a combination of bright-field and selected area diffraction modes in an electron microscope, the nanoscopic and microscopic structure of the new compound is fully characterized. It is found that the two-dimensional PBA forms small (hundreds of nanometers) single crystals, with the majority being true monolayers. The rest of the material is present in stacks of monolayers, which is likely to have occurred during deposition onto the substrate. These results constitute a proof-of-concept, and shows that PBA and other functional materials can be synthesized in two-dimensions by coordination restriction and the Langmuir-Schaefer technique.

# Zusammenfassung

Zweidimensionale Materialien an der Spitze der Materialforschung in den letzten zehn Jahren aufgrund der Tatsache, dass ihre physikalischen Eigenschaften sind oft ganz anders als ihre Groß Kollegen gewesen. Das macht sie eine spannende Ort, um zu erkunden, und viele Einzelschichten und dünnen Filmen haben Anwendungen als Plattform für Geräteanwendungen gefunden. Diese Arbeit kombiniert diese zweidimensionalen Welt mit einem anderen Spannungsfeld, Funktionskoordinationsverbindungen, durch die Synthese wirklich zweidimensionale Kristalle von Preußischblau-Analoga (PBA). Die Synthese wurde durch eine neue Variante der Langmuir-Schäfer-Technik, die eine zweidimensionale Oberfläche, auf der die forma Reaktion stattfinden kann, bietet, vermittelt. Zweidimensionalität wurde durch die Beschränkung der Koordinationsebene von einer der Vorläufer verhängt. Durch Verwendung einer Kombination von Hellfeld- und Bereichsbeugung Modi in einem Elektronenmikroskop wird die nanoskopische und mikroskopische Struktur der neuen Verbindung vollständig charakterisiert. Es zeigt sich, dass die zweidimensionale PBA bildet kleine (hundert Nanometer) Einkristalle, wobei die Mehrheit stimmt Monoschichten. Der Rest des Materials im Stapel von Monoschichten, die geeignet sind, während der Abscheidung auf das Substrat aufgetretenen vorliegt. Diese Ergebnisse stellen eine Proof-of-concept, und zeigt, daß PBA und andere funktionelle Materialien knnen in zwei Dimensionen durch Koordination Restriktion und der Langmuir-Schäfer-Technik synthetisiert werden.

# Acknowledgements

Although I may have written it, finishing this thesis was definitely a team effort. The first thanks, of course, needs to go to my beautiful wife Frans. She has been so patient and understanding of this whole process that I know I could never have gotten it done without her. My parents and brothers have been great too, making sure I remember to take a break from writing every once in a while.

As for the science, I would like to start by thanking my supervisor Dwayne. He has been so supportive and patient with dealing with the process of getting this thesis done. Hopefully the next thesis will go a little more smoothly!

Speaking of bureaucracy, Sonia Utermann's help has been indispensable for cutting through the red tape (and finding which tape to cut!).

This research was done in collaboration with Régis Y.N. Gengler and Andreas Rossos, both of whom always had time to discuss concepts and results with me. I would like to especially thank Régis for his guidance during this work.

Finally, I would like to thank my good friend Claudiu C. Gradinaru for his continuing support of my scientific career, which I always appreciate.

# Contents

# List of Figures

# List of Tables

# 1 Two-Dimensional Prussian Blue Analogues

## 1.1 Introduction

Materials science has progressed significantly since the early days of taking a substance and characterizing it in terms of its chemical constituents, atomic structure, and various other physical properties. As our understanding of chemical bonding and crystallography has matured in the last century, materials science has evolved past this "discovery" phase into a more controlled "design" phase, where novel materials are being constructed, atom by atom, to serve a tailored purpose. This has been an extremely successful effort, and a plethora of designer materials with exotic properties now exist, such as negative refractive index metamaterials[1], room-temperature superconductors[2], and tunable Dirac fermions[3].

This thesis attempts to unite the "discovery" and "design" paradigms of traditional materials science by presenting the synthesis and characterization of a new material. A novel compound, a two-dimensional Prussian blue analogue (PBA), was purposefully constructed to combine the strengths and unique properties of two exciting fields: two-dimensional materials and functional coordination compounds. This constitutes the design component of the research programme. The discovery component comes from the careful characterization of the newly synthesized compound, providing a thorough picture of its nanoscopic to microscopic structure.

Both low-dimensionality and coorsdination compounds are booming areas of research, and have been at the forefront of materials science for the last decade or so. In particular, two-dimensional materials show potential to revolutionize many aspects of modern technology, including field-effect transistors[4, 5], thermoelectronics[4, 5], optoelectronic memory[6], and even medical applications[7]. Traditional three-dimensional PBA has found many useful applications as well; biosensors[8, 9], battery cells[10], and displays and "smart"

windows[11] are just a few of the many areas in which PBA has made significant contributions. Because PBA plays such an imperative role in this thesis, more details on its synthesis and structure will be presented in the following section.

## 1.2 Functional Coordination Compounds: Prussian Blue Analogues

Prussian Blue Analogues (PBAs) are coordination materials of the form $D_nA_p[B(CN)_6]_q \cdot zH_2O$, where $n$, $p$, $q$, and $z$ are stochiometric numbers, D is an alkali cation, and A and B are transition metals ions. Popular choices for A and B are iron, nickel, manganese, or chromium. Traditionally, A is in a bivalent state, i.e. A(II), and B is in a trivalent state, i.e. B(III). This unique mixtures of valencies equips PBAs with a wide range of exotic properties which are tunable by the selection of the appropriate combination of transition metals. While the majority of these are magnetic properties as a result of the low spin and high spin states of A and B, respectively, several other unique physical properties have been demonstrated. Table 1.1 summarizes some of the most important properties that have been observed in PBA. These exotic characteristics makes PBA one of the most interesting and popular functional coordination materials.

Table 1.1: Compilation of some of the exotic properties of Prussian blue analogues

| Magnetic Properties | References |
|---|---|
| High $T_c$ magnetism | [12, 13] |
| Photo-magnetism | [14, 15] |
| Magnetic pole inversion | [16, 17] |
| Super paramagnetism | [18, 19] |
| Spin glass behaviour | [20] |
| Other Physical Properties | |
| Cyanide linkage isomerization | [21] |
| Negative and zero thermal expansion | [22–24] |
| Hydrogen storage | [25] |
| Electrochromic behaviour | [26, 27] |
| Photophysical behaviour | [28] |

The synthesis of PBA simply involves the slow mixing of two solutions; more precisely, it follows a classical Lewis acid-base reaction, as presented below:

$$q[\mathrm{B(CN)_6}]^{p-}_{aq}\,(\text{Lewis base}) + p\mathrm{A}^{q+}_{aq}\,(\text{Lewis acid}) \rightarrow \{\mathrm{A}_p[\mathrm{B(CN)_6}]_q\}^0 \cdot x\mathrm{H_2O}\,(\textit{solid}) \quad (1.1)$$

If done correctly, this reaction produces single crystals of PBA with the well-known structure shown in Fig. 1.1. PBA forms a face-centered cubic (FCC) lattice, with $[\mathrm{B(CN)_6}]$ occupying the corners and faces of the cube, and the metal A present at all the octohedral sites. The cyanide groups provide linkers between the alternating metal centers. If present, the cation D can be inserted in the tetrahedral sites of the cubic lattice, providing charge compensation[11]. Additionally, coordinated water molecules can fill $[\mathrm{B(CN)_6}]$ vacancies, depending on the stochiometry. The unit cell size is quite large, with the A-A distance ranging from 10 Å to 11 Å[29]. This large spacing enables some of the unique properties of PBA, in particular the hydrogen storage.

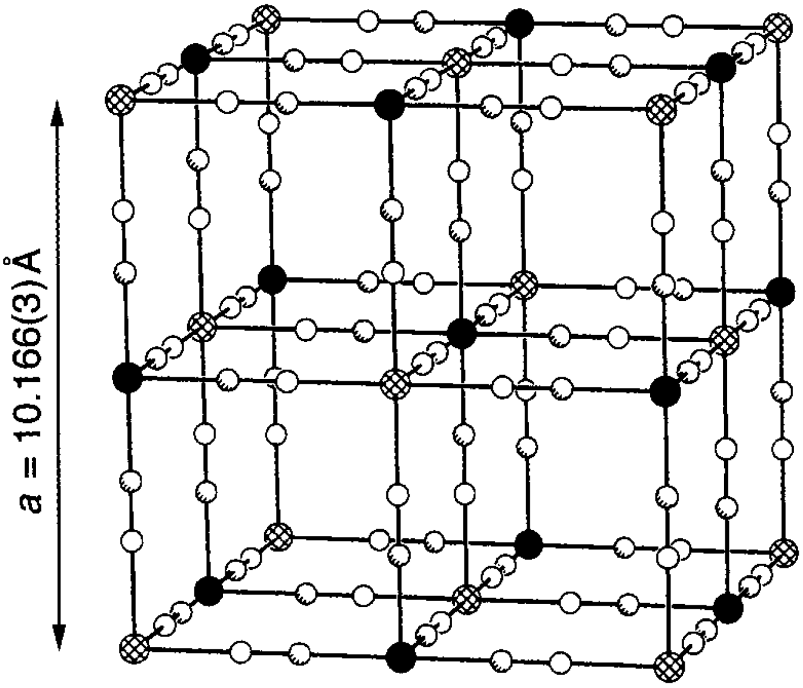


Figure 1.1: Unit cell of Prussian blue analogues (copied from [30]). Black, cross-hatched, shaded, and white spheres represent A, B, C, and N atoms, respectively. A typical unit cell parameter $a$ is shown (in this case, it corresponds to A=B=Fe).

While the synthesis follows a particularly elementary procedure, various more sophisticated approaches exist, such as electrochemical deposition[31–34], casting from colloidal solution[35], and dip coating[36]. Unfortunately, all of the these methods suffer from a lack of control over important parameters, such as film thickness and composition, which are vital for creating useful functional materials.

In light of this, recent studies[37, 38] using a Langmuir-Schaefer (LS) technique are extremely promising, and have shown great potential toward fabricating device quality PBAs. LS is a procedure that utilizes the liquid-air interface to enable precise control over the film thickness (number of layers deposited) with molecular level accuracy. This makes LS an extremely powerful approach for constructing designer functional materials. The technical details of LS are presented in Section 3.1. As will be highlighted in the following section, the control offered by LS is an imperative tool for the successful synthesis of two-dimensional PBA.

## 1.3 Two-Dimensional Prussian Blue Analogues

As is evident from Fig. 1.1, traditional PBA forms three-dimensional building blocks. To reduce the dimensionality of PBA and bring it into the two-dimensional world, the reaction in Eq.(1.1) and the crystal structure in Fig. 1.1 were carefully analyzed. This led to the realization that the inherent three-dimensional structure is imposed by the coordination level of the hexacyanide precursor. Therefore, it was hypothesized that using a precursor with a tetracyanide group would force the PBAs to form two-dimensional monolayers.

In a naive ball-and-stick model of the lattice structure the forces on each metal atom within the plane will be identical in the two-dimensional and three-dimensional cases. Even if the distribution of the electron density along the cyanide bridges is taken into account, the net out-of-plane forces on each metal atom will be approximately zero in both cases since it is absent in the two-dimensional case and cancels due to symmetry in the three-dimensional case. Therefore, it is expected that the in-plane structure of the two-dimensional PBA will maintain the same square arrangement. While it is possible for there to be some out-of-plane buckling, the planar square crystal maximizes the A-A distance, consistent with the repulsive Coulombic forces between the charged metal ions. Additionally, it is a well-established fact that tetracyanide compounds, in particular $Pt(CN)_4$, take planar geometries in crystal structures[39, 40]. In light of this and the argument based on coordination number restriction presented above, the structure of the two-dimensional PBAs can be anticipated, the result of which is shown in Fig. 1.2. The synthesis of such a two-dimensional PBA allows for stacks of materials to be built in the third dimension out of the monolayer building blocks by consecutive LS transfer.

In light of the structural arguments presented above, the goal of this thesis is to introduce and characterize a novel two-dimensional PBA with the general formula $D_nA_p[B(CN)_4]_q \cdot zH_2O$. This is done with the following reaction, that is analogous to Eq.(1.1):

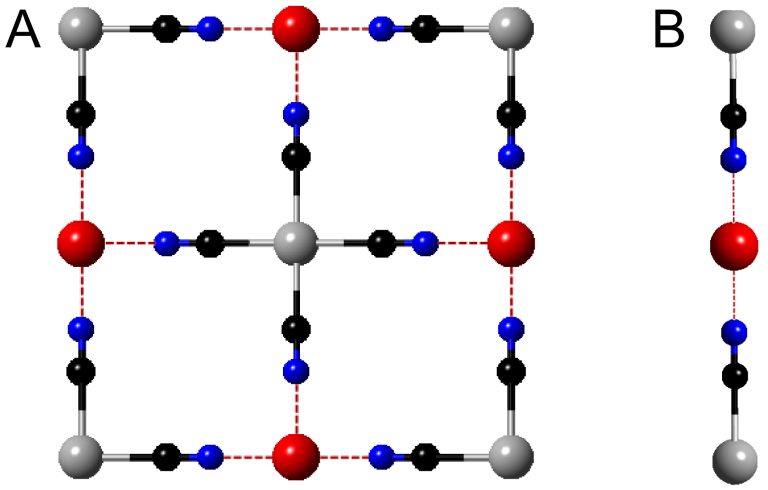


Figure 1.2: (A) Proposed unit cell of two-dimensional Prussian blue analogues. (B) Projection of unit cell in (A) revealing two-dimensional nature of structure. Red, gray, blue, and black spheres represent A, B, C, and N atoms, respectively.

$$q[\mathrm{B(CN)_4}]^{p-}_{aq} + p\mathrm{A}^{q+}_{aq} \rightarrow \{\mathrm{A}_p[\mathrm{B(CN)_4}]_q\}^0 \cdot x\mathrm{H_2O}\,(\mathit{solid}) \tag{1.2}$$

Successful synthesis of this material is enabled by the control offered through the LS technique. Although the water-air interface already provides a two-dimensional surface on which the above reaction can take place, a novel variant of LS, deemed "inverted" LS, was designed and used to ensure that a truly two-dimensional material is created at the interface. This method is presented in Section 3.1.

Based on the limited availability of appropriate tetracyanides, the chosen metals were copper for A and platinum for B, in the precursor forms of copper (II) chloride ($\mathrm{CuCl_2}$) and potassium tetracyanoplatinate(II) ($\mathrm{K_2Pt(CN)_4}$), respectively. This led to the final proposed reaction:

$$\mathrm{CuCl_2}\,(\mathit{solid}) \rightarrow \mathrm{Cu}^{2+}_{aq} + 2\mathrm{Cl}^{-}_{aq} \tag{1.3a}$$

$$\mathrm{K_2Pt(CN)_4}\,(\mathit{solid}) \rightarrow 2\mathrm{K}^{+}_{aq} + [\mathrm{Pt(CN)_4}]^{2-}_{aq} \tag{1.3b}$$

$$[\mathrm{Pt(CN)_4}]^{2-}_{aq} + \mathrm{Cu}^{2+}_{aq} \rightarrow \left\{\mathrm{Cu^{II}[Pt^{II}(CN)_4]}\right\}^0\,(\mathit{solid}) \tag{1.3c}$$

This 1:1 stochiometry is expected since both Cu and Pt are in bivalent cationic states[11], although this requires further investigation. Preliminary x-ray photoelectron spectroscopy (XPS) measurements[41] support this stochiometry, and also suggest a lack of extraneous alkali atoms and the absence of any vacancies in the lattice. However, these XPS results are not discussed further as the scope of this thesis is restricted to the nanoscopic and microscopic structure of the two-dimensional PBA crystals.

## 1.4 Outline of Thesis

The remainder of this thesis is comprised of five chapters, each dedicated to an isolated part of the experimental details or results of the research. All of the conclusions reached about the nature of the two-dimensional PBA crystals are a consequence of careful analysis of transmission electron microscope (TEM) measurements, both in bright-field and selected area diffraction modes. Accordingly, the following chapter is devoted to introducing the general operating principles behind electron microscopy, in addition to outlining the mathematical details behind the quantitative analysis of TEM images and diffraction patterns. The specific experimental details used to record and process the TEM data is presented in Chapter 3. The next two chapters, Chapters 4 and 5, contain the novel contributions from this thesis. Detailed results from the TEM data are presented, and some conclusions about the nanoscopic and microscopic structure of the two-dimensional PBA are drawn. Finally, the remaining chapter summarizes the results and distills them into a consistent picture of the structure of the two-dimensional PBA crystals.

# 2 Transmission Electron Microscopy

## 2.1 Introduction

Understanding the structural properties of the two-dimensional PBAs is an important step towards their full characterization. To this end, transmission electron microscopy (TEM) was employed to identify both the crystallite properties and crystal structure of the two-dimensional PBA. This chapter will outline the important concepts of TEM use, as well as briefly introduce the pertinent theory.

Transmission electron microscopy is a powerful microscopy technique that passes a beam of electrons through a thin sample in order to glean structural information at high magnification. The ultimate goal of any microscopy measurement is to be able to observe individual atoms, and so the limiting factor to the success of microscopy is its spatial resolution. For all microscopes (visible-light, electron, x-ray, etc.), the resolution is given by Rayleigh's criterion[42] as

$$\text{resolution} \approx \frac{\lambda}{2\,\text{NA}} \tag{2.1}$$

where NA is the numerical aperture of the delivery system and $\lambda$ is the wavelength of the probe. While the maximizing the numerical aperture may be a design challenge, the true bottleneck to achieving atomic resolution is the wavelength. According to Eq.(2.1), the resolution is proportional to the wavelength of the probe; that is, a probe with a small wavelength could significantly improve the spatial resolution of the microscope. Unfortunately, optical microscopes have wavelengths in the visible spectrum (400 – 700 nm) which limits their resolution to a few hundred nanometers.

TEMs were developed to combat this limitation by taking advantage of the wave-like nature of electrons to push the resolution limit to the sub-nanometer regime. Electrons, like all matter, possess both wave- and matter-like qualities, as ascribed by the current

understanding of quantum mechanics. The associated de Broglie wavelength of an electron accelerated by a potential $U$ is

$$\lambda = \frac{h}{\sqrt{2m_e qU + \frac{q^2U^2}{c^2}}} \tag{2.2}$$

where $h$ is Planck's constant, $q$ is the elementary charge, $m_e$ is the electron's rest mass, and $c$ is the speed of light in vacuum (see Table 2.1 for the numerical values of the pertinent fundamental constants). This expression accounts for relativistic effects, which is important because electrons in typical TEMs travel near the speed of light. This is evident in Fig. 2.1, which shows the wavelength and speed of an electron in a TEM as a function of its acceleration voltage. Evidently, electrons accelerated by $U = 100$ kV travel at about $0.5c$, highlighting the importance of the relativistic correction. Modern TEMs operate with acceleration voltages of 200–400 kV, resulting in typical spatial resolutions of 0.1 - 0.3 nm[42, 43].

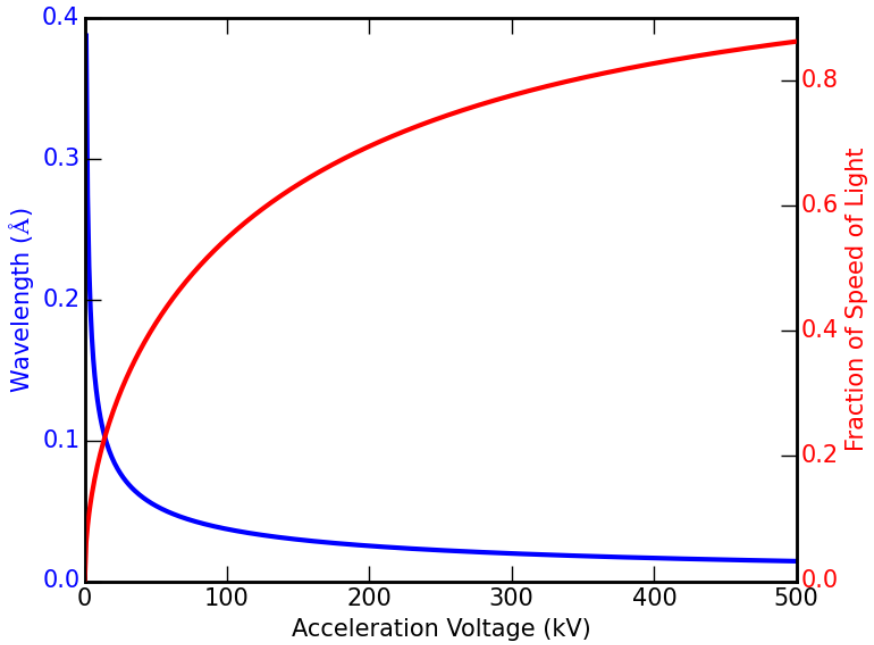


Figure 2.1: The dependence of the wavelength and speed of electrons in a transmission electron microscope on the acceleration voltage, accounting for relativistic effects.

A simplified version of the layout of a conventional TEM is given in Fig. 2.2. Besides the electron source and the sample holder, the crucial components are a series of magnetic lenses and apertures responsible for illuminating the sample and imaging the scattering, and also the detector system. The detector typically consists of a phosphor screen coupled to a CCD camera. State-of-the-art machines contain several other lens and components

Table 2.1: Numerical values of several fundamental constants relating to transmission electron microscopy

| Fundamental Constant | | |
|---|---|---|
| Name | Symbol | Value |
| Planck's constant | $h$ | $6.626 \times 10^{-34}$ J·s |
| elementary charge | $q$ | $-1.602 \times 10^{-19}$ C |
| electron rest mass | $m_e$ | $9.109 \times 10^{-31}$ kg |
| speed of light in vacuum | $c$ | $2.998 \times 10^{8}$ m/s |

that are responsible, for instance, for aberration correction and beam steering. Additionally, most of the elements typically consist of more than a just pair of cooperating lenses. For a discussion of the layout of modern TEMs, please see [42, 43].

Contemporary TEM designs offer the versatility of several different measurement modes, and the positioning of the optical elements and the electron beam path depend on the mode employed. To study the two-dimensional PBAs, both the bright-field imaging and selected area diffraction modes were used. Each of these will be discussed individually in the following section.

## 2.2 Bright-field Imaging

Bright-field imaging is the conventional imaging mode, analogous with optical compound microscopy. The electron beam travels the path shown in the left side of Fig. 2.2. After the electron source, a series of condenser lenses collects and collimates the electrons onto the sample after passing through a condenser aperture to clean the beam. The electrons then scatter from the sample, and are collected with an objective lens close to the sample. An objective aperture is placed in the back focal plane of the (lower) objective lens and is used to select the (000) transmitted beam. This improves the contrast in the image by removing the influence of any scattered electrons. Finally, the rest of the imaging system, ending with a projector lens, images the beam onto the detector with the desired magnification. As was mentioned previously, this is a rather simplified presentation of the true beam path within the TEM; a more complete discussion can be found in any number of textbooks on TEM operation[42, 43].

Bright-field imaging is based on the principle of amplitude (diffraction) contrast, which works in the following way: scattering from the sample removes intensity from the direct, transmitted beam. Because the objective aperture blocks these scattered electrons, the de-

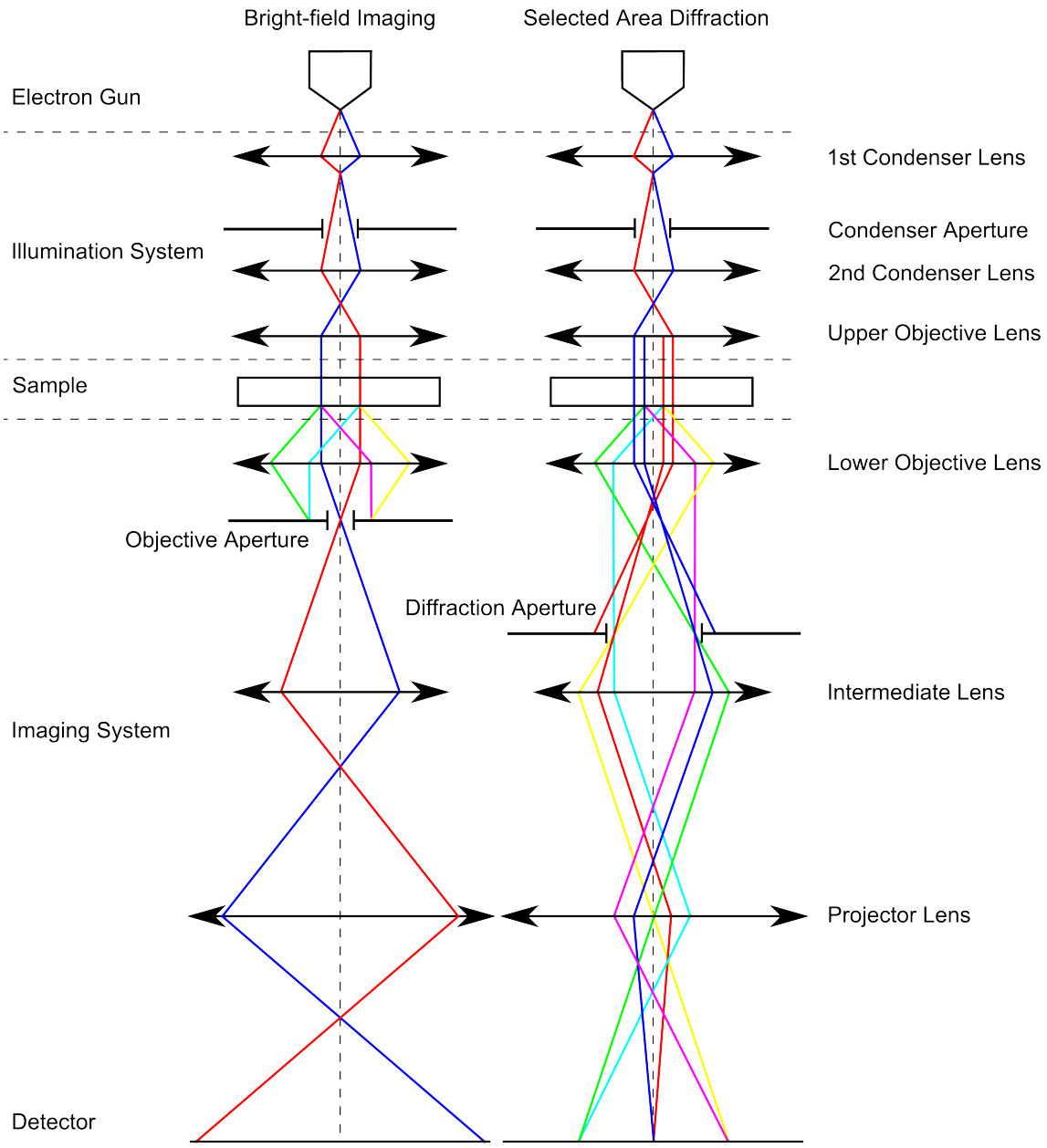


Figure 2.2: Schematic layout of a transmission electron microscope showing the beam path for bright-field imaging and selected area diffraction modes

tected image, formed from the transmitted beam, will have a lower intensity than the incident beam. Because the scattered intensity is proportional to the sample thickness[42, 43], this then enables a method for imaging the sample: in thicker regions of the sample, the image will be less intense because more electrons have been removed from the transmitted beam due to the increased scattering. Similarly, thinner parts of the sample transmit more electrons, and so will appear brighter on the detector (hence the name "bright-"field imaging).

Drawing an analogy to optical imaging leads to the following equation for the intensity,

$I$, of the transmitted beam through the sample:

$$I = I_0 \exp(-\mu t) \tag{2.3}$$

where $I_0$ is the incident intensity, $\mu$ is the linear attenuation coefficient, and $t$ is the sample's thickness. The attenuation coefficient accounts for all interactions with the sample through the total scattering cross section $\sigma^{tot}$, which includes contributions from both elastic and inelastic scattering. For a crystalline sample consisting of several distinct types of atoms in its unit cell, the two are related by

$$\mu = \sum_i \sigma_i^{tot} N_i \tag{2.4}$$

where the sum runs over all distinct types of atoms in the unit cell, $\sigma_i^{tot}$ is the total scattering cross section corresponding to the $i^{th}$ atom type, and $N_i$ is the number of the $i^{th}$ type of atom per unit volume. To arrive at this equation, each atom has been treated as an isolated scattering center and has had its contribution added incoherently.

Because the collection of the scattered electrons is limited by the objective aperture (see Fig. 2.2), the total scattering cross sections only need to account for scattering greater than an angle $\beta$, defined by the collection angle of the objective aperture. That is, if $d\sigma^{tot}/d\Omega$ is the total differential scattering cross section, we are concerned with

$$\sigma_i^{tot}(\beta) = 2\pi \int_\beta^\infty \frac{d\sigma^{tot}}{d\Omega} \sin\theta \, d\theta \tag{2.5}$$

Additionally, the total scattering cross section must include contributions from both elastic ($el$) and inelastic scattering ($inel$), and so the final expression for the cross section is

$$\sigma_i^{tot}(\beta) = \sigma_i^{el}(\beta) + \sigma_i^{inel}(\beta) \tag{2.6}$$

Eq.(2.3) is the general expression governing image formation in bright-field imaging; accordingly, spatial variation in the sample thickness ($t$), the structure ($N$), or the chemical composition ($\sigma$) therefore leads to contrast in the bright-field image.

Bright-field imaging is well suited for obtaining high resolution images at moderate mag-

nification. It will be used to measure the size and shape of the two-dimensional PBA nanocrystallite domains, the results of which are discussed in Chapter 5.

## 2.3 Selected Area Electron Diffraction

If the sample of interest has a crystalline structure, then the scattered electrons form a diffraction pattern which can be measured in the TEM. The electron beam is incident on a small area on the sample (typically around 200 nm[42, 43]), so that the structural properties of a spatially-localized area can be measured. This mode is used to study the crystal structure of individual two-dimensional PBA nanocrystals, as presented in Chapter 4.

Operation in this mode is similar to that of bright-field mode, with the major difference being the aperture positioning (see the right side of Fig. 2.2). To operate in this mode, the electron beam is delivered collimated to the sample by adjusting the condenser lens properties (see Fig. 2.2). The other significant difference compared with the bright-field mode is that the objective aperture is fully removed from the beam, and instead replaced with a diffraction aperture in the image plane of the objective lens. This aperture limits the effective spot size on the sample. The diffraction pattern is then projected onto the detector.

At this point it is important to distinguish between polycrystalline samples and single-crystals. Materials that form single-crystals have an undisturbed periodic structure over the entire volume of the sample. The pattern formed in the diffraction mode in a TEM of such samples contains spots arranged in a regular pattern (see Fig. 2.3). This is in contrast with polycrystalline samples, which are composed of many individual single-crystals (called crystallites or nanocrystals) at random orientations to each other (see Fig. 2.3 B). In this case, the diffraction pattern of each individual crystallite is rotated according to its orientation, and so the measured diffraction pattern contains rings (which may or may not have a uniform intensity around the ring depending on if all orientations are equally sampled).

Structural information is contained in both the location and the shapes of diffraction spots/rings. Because diffraction rings were observed for two-dimensional PBA (see Chapter 4), we will limit our discussion to polycrystalline samples. The general approach for analyzing polycrystalline diffraction patterns begins with averaging the patterns about the angular coordinate; because of the angular symmetry, this improves the signal to

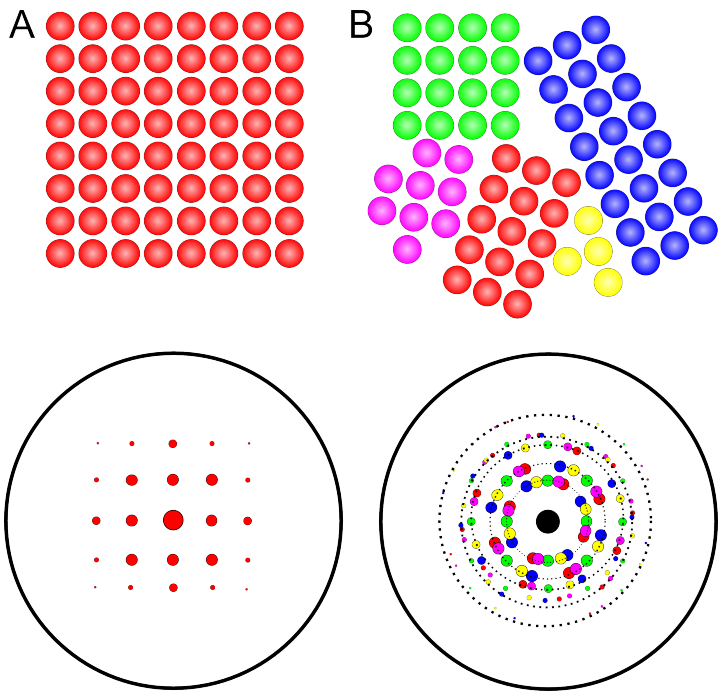


Figure 2.3: (A) A single-crystal (top) and its corresponding diffraction pattern (bottom). (B) A polycrystalline sample composed of many single-crystals (top) and its corresponding diffraction pattern (bottom). Each individual single-crystal in the polycrystalline sample has been coloured separately to distinguish it.

noise without any loss of information. The resulting radial diffraction pattern, $I(2\theta)$, contains an array of diffraction intensities as a function of the scattering angle $2\theta$. The theory behind the quantitative analysis of radial diffraction patterns will be outlined in the following sections.

### 2.3.1 Width of Diffraction Rings from Polycrystalline Samples

The widths of the diffraction rings contain information about structural imperfections in the crystal. Here the "width" of a peak centered at $2\theta$ is taken to be integral breadth

$$\beta(2\theta) = \frac{1}{I_{max}(2\theta)} \int_{2\theta-\epsilon}^{2\theta+\epsilon} I(2\theta) d\,(2\theta) \tag{2.7}$$

where $I(2\theta)$ is the radial diffraction pattern and $\epsilon$ is chosen to encompass the entire peak. There are two significant factors contributing to this width (after instrument broadening has been accounted for): the finite size of the nanocrystals, and the strain leading to distortions from a perfect crystal structure in each individual crystallite. The width induced by the former is described by the Scherrer equation[44]:

$$\beta_{size}(2\theta) = \frac{K\lambda}{L\cos\theta} \tag{2.8}$$

where $K = 2\sqrt{\ln 2/\pi} \approx 0.94$ for cubic crystals and $L$ is the average "size" of the nanocrystallite.

Strain refers to the fact that each individual crystallite might not be exactly a perfect crystal. It can be broadly characterized in terms of *uniform*, and *non-uniform* strain. Uniform strain accounts for the fact that the spacing between the lattice planes might be slightly larger or smaller for all the crystals compared with the theoretical value. In the absence of any strain, the momentum transfer $q$ that interferes constructively to produce diffraction peaks is $q = 2\pi/d$, where $d$ is the distance between the lattice planes. The presence of uniform strain thus implies that as $d$ increases, $q$ decreases, and vice versa. Non-uniform strain describes the situation where each crystal might have different spacing, but the overall average lattice plane spacing is the theoretical value. That is, $d$ varies for each crystallite, but the ensemble average satisfies $\langle d \rangle = d$. This means that the positions of the diffraction peaks will not change, but the width of the peaks will increase. By differentiating Bragg's law, $2d\sin\theta = \lambda$, we get

$$\Delta(2\theta) = 2\left(\frac{\Delta d}{d}\right)\tan\theta \tag{2.9}$$

where $\Delta(2\theta) = \beta_{strain}(2\theta)$ is the full-width-at-half-maximum of the diffraction ring. The term $\Delta d$ can be identified in terms of the distribution $p(e)$; if $p(e)de$ is the fraction of the crystal with tensile strain between $e$ and $e + de$[45], then we can identify $\zeta = \Delta d/d$ as the integral breadth of $p(e)$ (analogous to the definition in Eq.(2.7)). The width induced by microstrain in the crystal is therefore given by $\beta_{strain}(2\theta) = 2\zeta\tan\theta$.

The total peak shape is a convolution of the lineshape from both the size and strain effects. Both Lorentzian and Gaussian functions were used to fit the diffraction peaks, and it was found that a Lorentzian lineshape resulted in minimal residuals. In this case, the total integral width is

$$\begin{aligned}\beta(2\theta) &= \beta_{size}(2\theta) + \beta_{strain}(2\theta) \\ &= \frac{K\lambda}{L\cos\theta} + 2\zeta\tan\theta\end{aligned} \tag{2.10}$$

Thus a plot of $\sin\theta/\lambda$ versus $\beta\cos\theta/\lambda$, as suggested by Williamson and Hall[46], is linear with a slope of $2\zeta$ and and intercept of $K/L$.

## 2.4 Conclusion

This Chapter introduced the main experimental and theoretical methodology used to study the two-dimensional PBAs. Both the diffraction and bright-field imaging modes of a transmission electron microscope were discussed, and the type of information accessible to each of these techniques was presented.

# 3 Experimental Methods

## 3.1 Langmuir-Schaefer production of Prussian Blue Analogue films

The two-dimensional PBAs were formed using a novel variant on the traditional Langmuir-Schaefer (LS) procedure, christened "inverted" LS. This technique is not unique to this thesis, but has been outlined in [41, 47]. For completeness, a brief introduction to this method will be presented.

Traditional LS involves forming monolayer films at the liquid-air interface by taking advantage of hydrophobic/-philic forces and surface tension. In the case of PBA, copper chloride ($CuCl_2$) was dissolved in water and used to fill a hydrophobic trough (see Fig. 3.1 A). An aqueous solution of potassium tetracyanoplatinate(II) ($K_2Pt(CN)_4$) was then slowly injected at the liquid-air interface, allowing the reaction in Eq.(1.3) to take place on the surface. Barriers on either side of the trough are then slowly closed to compress the product into a film. Inverted LS is a variation on this traditional procedure by instead starting with the barriers closed, creating a restricted area on which the formation of PBA can take place (see Fig. 3.1 B). The $K_2Pt(CN)_4$ is again added drop-wise, except this time with a glass slide half submerged in the subphase to allow a more "gentle" reaction to take place. As material is formed at the interface, the barriers are free to move and slowly opened to compensate for the newly covered surface area. This approach leads to a more uniform creation of films at the interface[41, 47]. Finally, the films are transferred to the desired substrate by horizontally dipping the substrate into the liquid.

It should be noted that control experiments were made during the sample preparation to ensure that the final film was composed of only PBA. Depositions of LS films were performed using only $CuCl_2$, and also using only $K_2Pt(CN)_4$, and both bright-field and diffraction TEM measurements confirmed that no sample was deposited in either case. This establishes that film formation only occurs if both reactants are present. Addi-

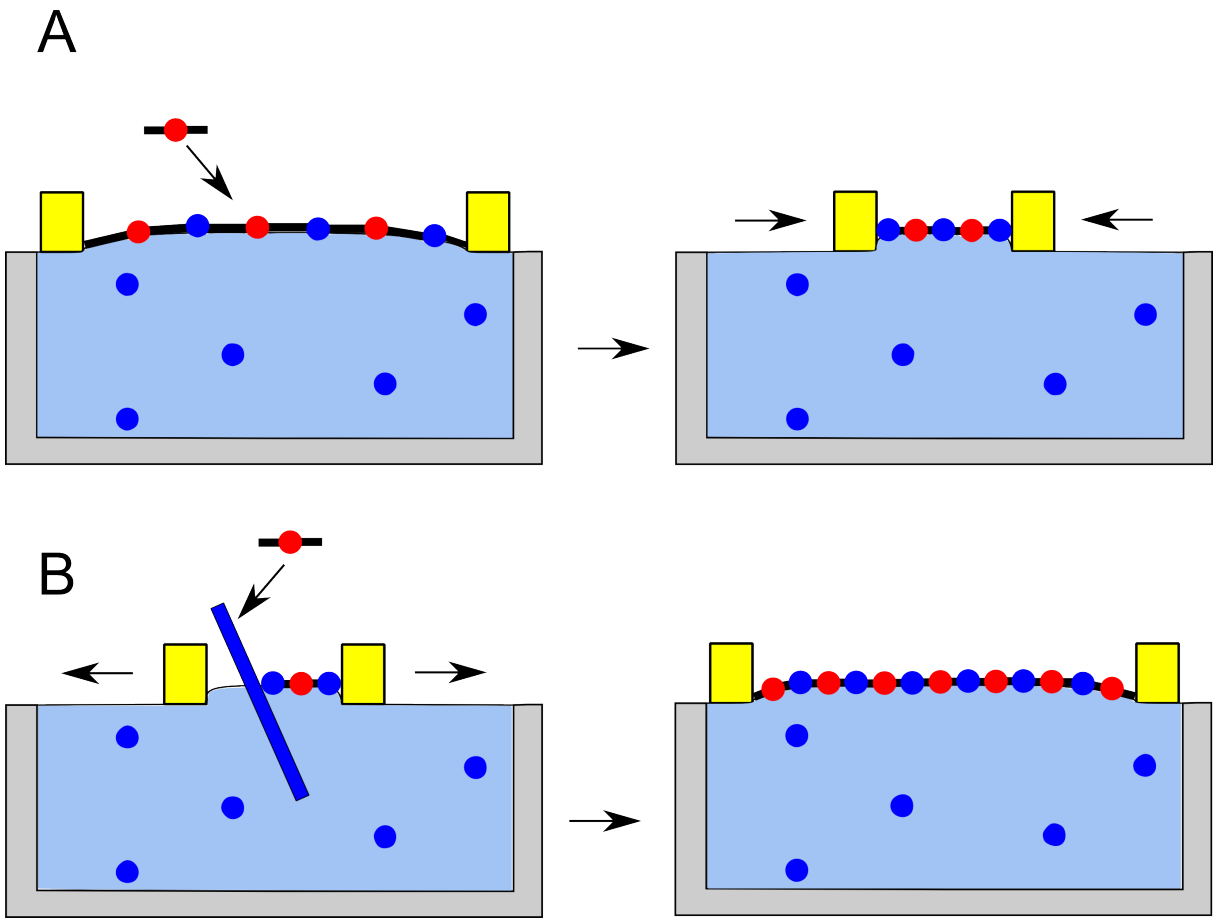


Figure 3.1: Schematic illustrations of the traditional (A) and inverted (B) Langmuir-Schaefer methods. Blue circles represent the copper ions in the subphase, and the red circles and black bonds represent the tetracyanoplatinate groups.

tionally, x-ray photoelectron spectroscopy (XPS) measurements were performed and confirmed the chemical composition of the PBA films, the results of which are presented in [41]. The conclusion was that the films were absent of any precursor (i.e. Cl or K).

## 3.2 Transmission Electron Microscopy

After the formation of the films, the two-dimensional PBAs were transferred to several different substrates to be studies in a TEM. Copper meshes with various hole sizes (ranging from 50 lines/inch to 2000 lines/inch) were tried, but minimal material was found to be deposited. When material was observed, it was almost always attached to the bars of the mesh. This suggests that the single-crystals formed were smaller than $\approx 1\mu$m, as they most likely fell through the holes during deposition. Based on this result, PBA was deposited on an untreated, 5 nm thick amorphous silicon nitride ($Si_3N_4$) film suspended

over windows on silicon frame (Plano GmbH). These windows are thin enough that the electrons in the TEM could still pass through them, but form a continuous support to hold the PBA films.

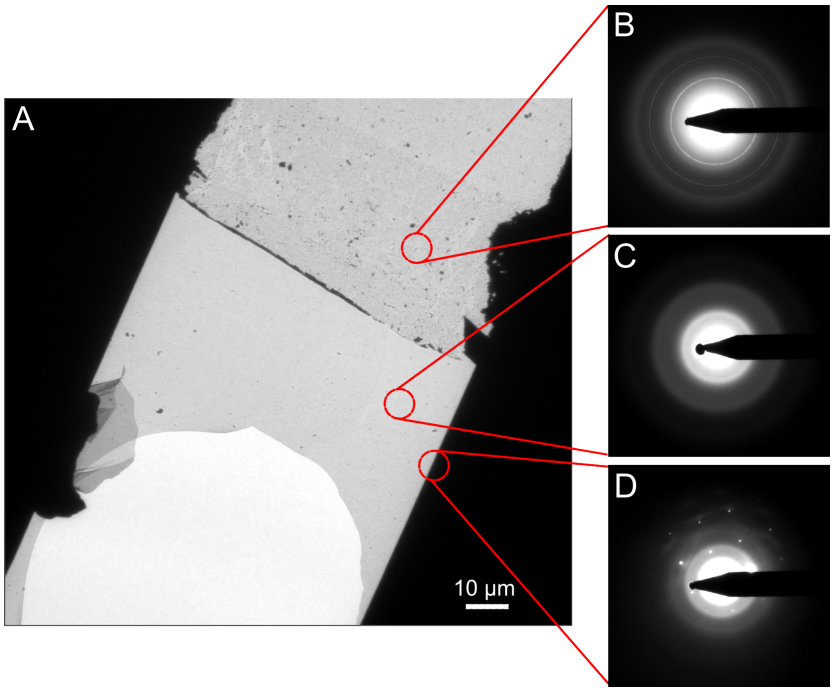


Figure 3.2: (A) Low-magnification bright-field TEM image of PBA deposited on a thin silicon nitride film atop a silicon frame. The bright part in the bottom left of the image is a region in which the silicon nitride film was broken. Representative diffraction patterns are shown for a region containing PBA atop of the silicon nitride substrate (B), silicon nitride in the absence of PBA, and the silicon frame (D).

TEM measurements were performed at room temperature with a Philips CM12 microscope operating at 80 kV ($\lambda = 0.0418$ Å). The basic measurement procedure was as follows: the microscope was first calibrated by examining the diffraction pattern from a polycrystalline gold sample. A significant amount of scattering was present due to the amorphous silicon nitride background; in bright-field imaging mode this is in the form of a uniformly intense background (see Fig. 3.2 A). In diffraction mode, the silicon nitride contributes a broad, featureless diffraction pattern (see Fig. 3.2 C). This was measured from a substrate without deposition, and was directly subtracted from the angularly averaged diffraction patterns of PBA. Finally, the remaining diffuse background due to inelastic scattering in the angularly averaged diffraction patterns was estimated using the Sonneveld-Visser algorithm[48] and subtracted.

Because the microscope's calibration is such an important aspect of the accurate and thorough analysis of the two-dimensional PBA structure, it will be discussed in-depth in the following section.

## 3.3 TEM camera length calibration

Calibration of the TEM is an imperative step to ensure that bright-field images can be accurately scaled and diffraction patterns can be faithfully indexed. Due to small variations in the sample position due to (for instance) hysteresis in the sample manipulators and changes in the magnetic lenses' resistance over time, the camera length is the main target for calibration. Although the camera length is reported internally by the the TEM, it is important to verify it through an external measurement. To perform such a calibration, a sample with a very well-known structure is examined in the TEM. The sample itself is inconsequential; what is important is that its structure has been measured extremely accurately using one or more independent methods. Typically a crystalline metal is used due to its strong scattering of the electrons and its long-term stability and robustness. In this case, a polycrystalline gold sample was used (see Fig. 3.4).

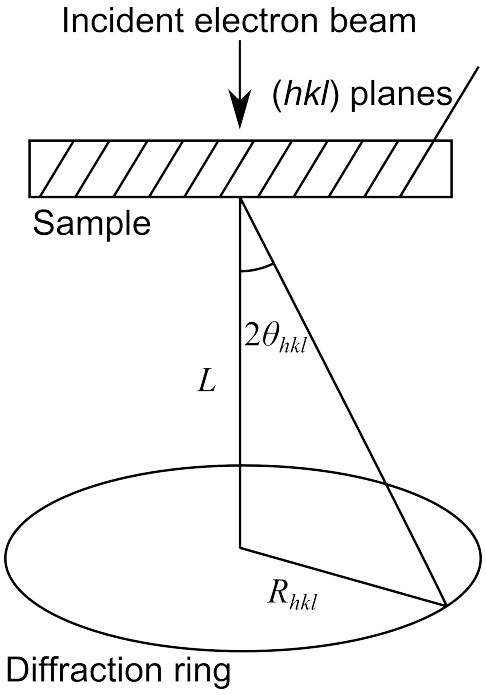


Figure 3.3: The geometry of the diffraction mode of a transmission electron microscope showing the relationship between the camera length $L$ and the scattering angle $\theta_{hkl}$ and diffraction ring radius $R_{hkl}$ of the $(hkl)$ reflecting plane.

Using simple geometry (see Fig. 3.3) one can deduce that the camera length $L$ and the scattering angle $\theta_{hkl}$ of a ring of radius $R_{hkl}$ are related according to $\tan(2\theta_{hkl}) = R_{hkl}/L$. Combining this with Bragg's law $2d_{hkl}\sin\theta_{hkl} = \lambda$, the camera length can be expressed in terms of lattice plane spacing $d_{hkl}$:

$$L = \frac{R_{hkl}}{\tan\left[2\sin^{-1}\left(\frac{\lambda}{2d_{hkl}}\right)\right]}. \tag{3.1}$$

Since the structure of gold is well-established to be face-centered cubic (FCC)[49], the lattice planes have the simple expression $d_{hkl} = a/\sqrt{h^2+k^2+l^2}$ where $a$ is the unit cell parameter. Thus the desired relationship between the camera length and an accurately measured structural parameter (the unit cell parameter) is arrived at:

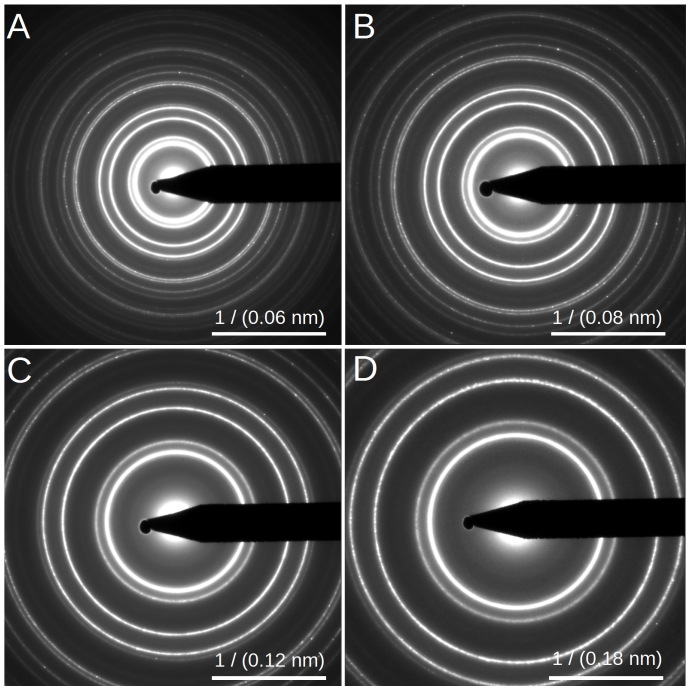


Figure 3.4: Diffraction patterns of a 30 nm thick polycrystalline gold film with varying magnifications used for calibrating a transmission electron microscope.

$$L = \frac{R_{hkl}}{\tan\left[2\sin^{-1}\left(\frac{\lambda\sqrt{h^2+k^2+l^2}}{2a}\right)\right]} \tag{3.2}$$

The complete procedure for the TEM calibration was the following: first, the angular average of the polycrystalline gold diffraction pattern was calculated and the peaks were identified. The peaks were indexed by sorting the peaks in ascending order by radius and matching them with the lowest order allowed Bragg reflections. For gold (and other FCC crystals), allowed reflections are whenever $(h, k, l)$ are either all odd or all even, as listed in Table 3.1.

Using the accepted value of $a = 407.82$ pm for gold[50], Eq.(3.2) was then used to calculate the camera length for each reflection, as shown in Fig. 3.5. Using several reflections improved the estimation of $L$ by providing some statistics. These values were averaged to give the calibrated camera length as $L = 164.2 \pm 0.19$ mm. The internal camera length

Table 3.1: Allowed reflections of gold

| $(h,k,l)$ | $\sqrt{h^2+k^2+l^2}$ |
|---|---|
| (1,1,1) | 1.73 |
| (2,0,0) | 2 |
| (2,2,0) | 2.83 |
| (3,1,1) | 3.32 |
| (2,2,2) | 3.46 |
| (4,0,0) | 4 |
| (3,3,1) | 4.36 |
| (4,2,0) | 4.47 |
| (4,2,2) | 4.90 |
| (3,3,3) | 5.20 |
| (4,4,2) | 6 |
| (5,3,3) | 6.56 |
| ⋮ | ⋮ |

reported by the TEM was 260 mm; it is evident that there is a significant variation, which highlights the importance of performing a calibration measurement each time the TEM is used.

## 3.4 Conclusion

The PBA films were produced with the Langmuir-Schaefer method, and subsequently studied using transmission electron microscopy. Some technical aspects of these two methods were outlined in this chapter, with emphasis placed on the proper calibration of the TEM's camera length. These discussions lay the groundwork for the quantitative results presented in the following chapters.

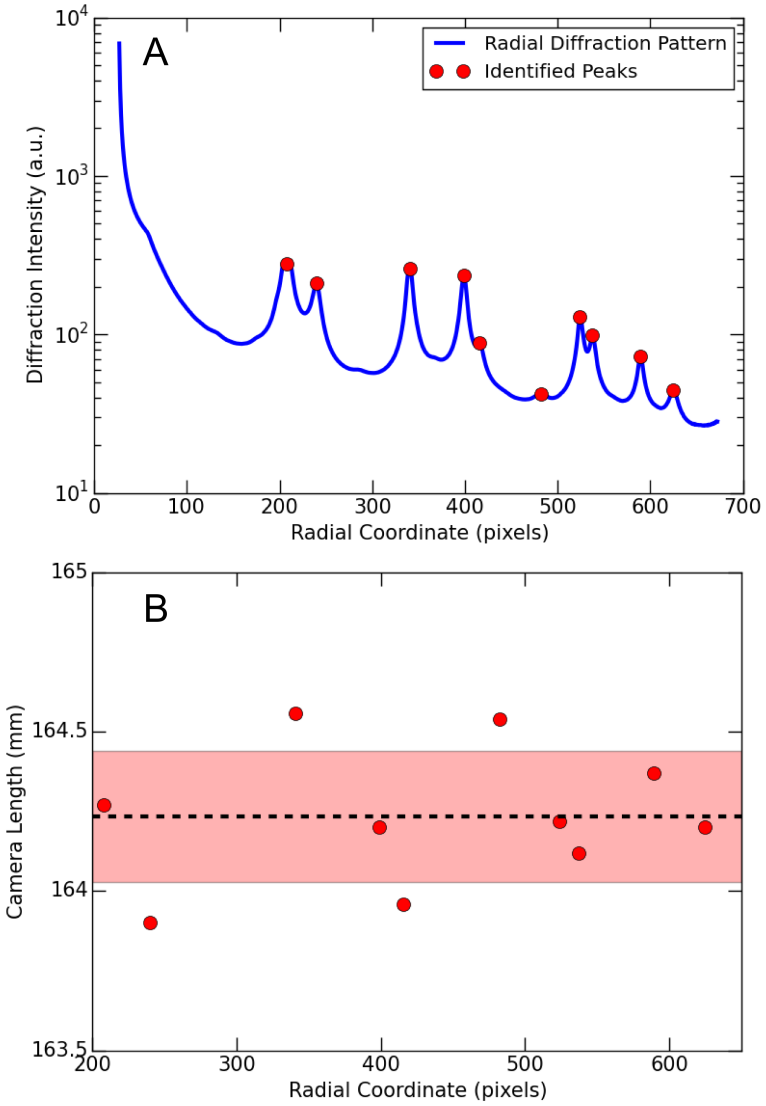


Figure 3.5: (A) Radial diffraction pattern of polycrystalline gold, with the peaks used for the camera length calibration identified. (B) Camera length calculated for each peak identified in (A), with the average value and standard deviation shown by the dashed line and the shaded region, respectively.

# 4 Results: Selected Area Electron Diffraction

The arguments based on coordination number restriction in Section 1.3 (and the bright-field images presented in the following chapter) allude to the two-dimensional nature of the PBA films. To complement these results and form a more complete understanding of the structural properties of the PBAs, selected area electron diffraction measurements were performed in the TEM. To get a good sampling over the distribution of nanocrystals, diffraction patterns were measured from several different samples and multiple regions on each sample.

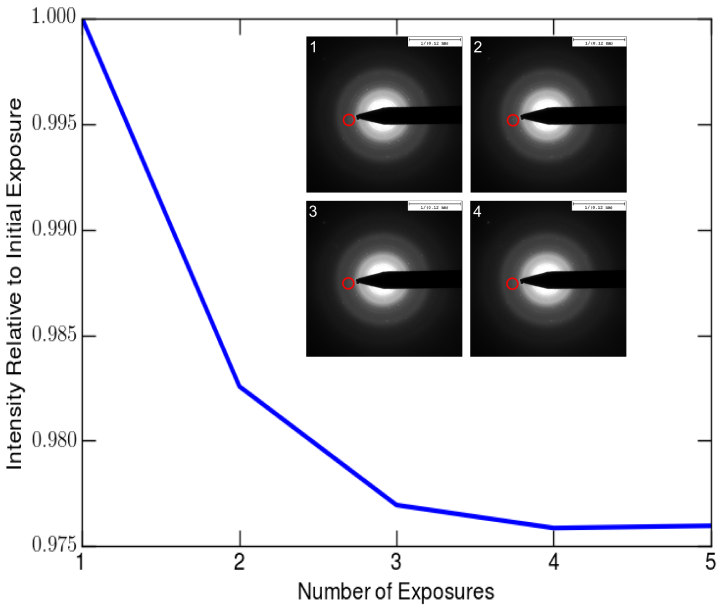


Figure 4.1: Intensity of indicated region of interest as a function of exposure to the TEM electron beam. Inset: Sequential diffraction patterns from the same sample area.

The images in Fig. 4.1 show several diffraction patterns measured in sequential order over the span of a couple of minutes from the same sample position, and the intensity of

the indicated region of interest. It is evident that the diffraction patterns faded in time due to the exposure to the electron beam, which is indicative of sample damage either by ionization or melting due to the beam current. Although the exact mechanism by which beam damage occurs is complicated and still under debate[42, 43], a simple explanation could be that inelastic scattering leads to energy transfer to the sample, thus producing heat or ionization. Although the cross section for inelastic scattering is small relative to that for elastic scattering, the high beam current in a TEM means that a significant number of inelastic events occurred. This is not an issue for robust samples; however, the cyanide bridges of two-dimensional PBA are known to be weak because the large unit cells results in a reduction or "thinning" of the electron density in the bonds due to electronic delocalization between the metal sites across the bridging cyanide anion[21] . In fact, electron beam induced damage has also been observed in traditional three-dimensional PBAs[51, 52]. Thus the presence of damage in the synthesized material is evidence for the existence of cyanide bridges in the two-dimensional PBA, in support of the proposed structure. As a result of this damage, typically only a few measurements could be made at each sample area.

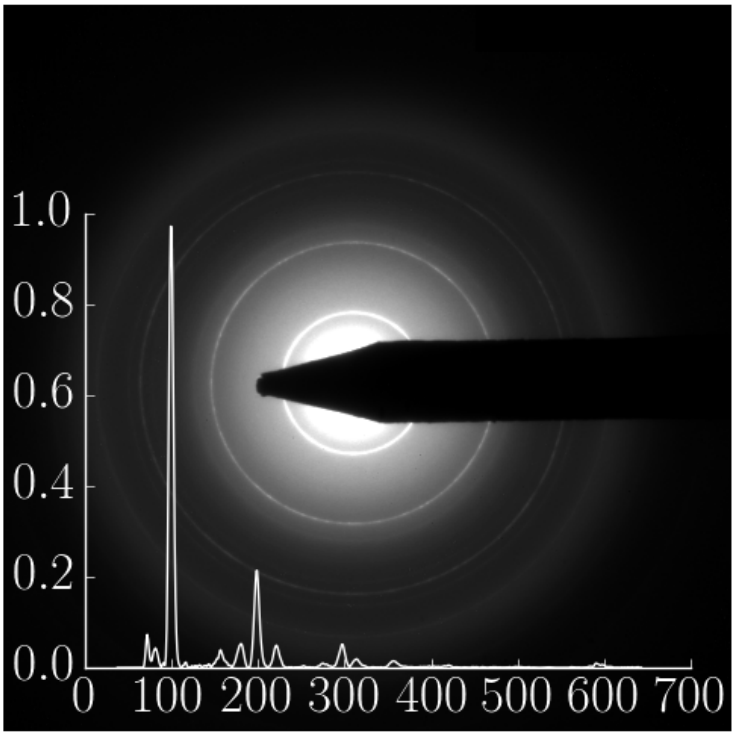


Figure 4.2: Representative polycrystalline diffraction pattern from a collection of two-dimensional PBA nanocrystals and the corresponding background-subtracted radial profile

A typical selected area electron diffraction pattern is shown in Fig. 4.2. This is a representative pattern formed by diffracting from many flakes (such as the bright-field images shown in Fig. 5.1). The broad, diffuse rings are due to scattering from the silicon nitride window. The sharp peaks suggests that that each flake is crystalline, although with a random azimuthal angle relative to its neighbours, such that a collection of flakes results in a polycrystalline pattern.

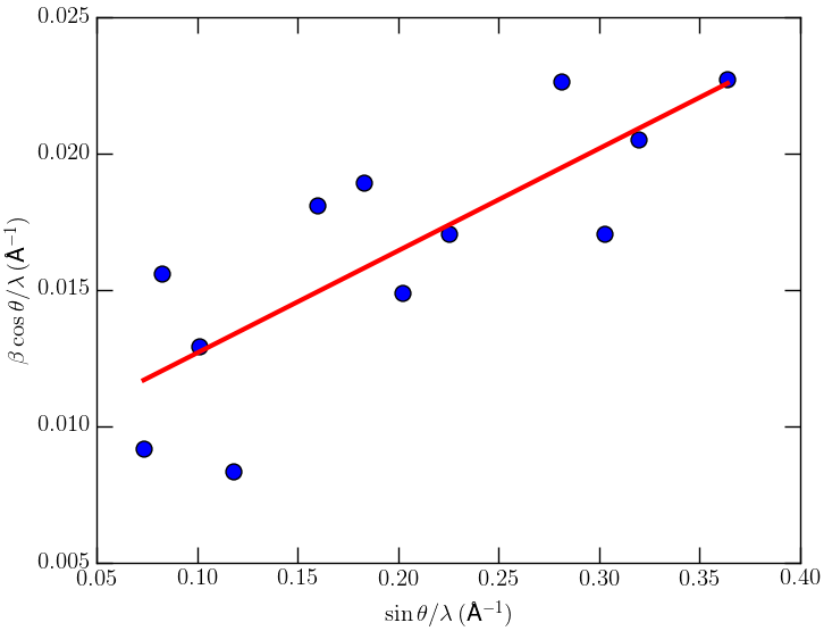


Figure 4.3: Williamson-Hall plot identifying the effect of the nanocrystalline size and strain on the integral width of the diffraction rings from a polycrystalline sample of two-dimensional Prussian blue analogues.

The widths of the diffraction peaks contain information about structural imperfections in the crystals. For the majority of materials, the most significant contributing factors are the finite size of the crystalline domains and the strain leading to distortions from a perfect crystal structure. These effects can be identified by their different dependencies on the scattering angle, with the peak widths proportional to $1/\cos\theta$ and $\tan\theta$, respectively. For a thorough discussion of these effects, refer to Section 2.3.1. By analyzing the peaks in the polycrystalline diffraction pattern with a Williamson-Hall plot (Fig. 4.3), we determine that the strain is $7.5 \pm 2.1$ %, and the average size is $10.5 \pm 2.6$ nm. It is important to emphasize that the size determined by such an analysis cannot be interpreted as the true size of the flakes, but rather corresponds to an effective coherence length of the crystalline domains. It represents a lower bound on the particle size, as is evident from the fact that it is significantly smaller than the flake size observed in the bright-field images (see the analysis in Chapter 5). This size is similar to what has been measured in three-dimensional PBAs[53]. The measured strain is quite large relative to traditional PBAs,

which is typically around 1 %[53]. This is likely due to two contributions: first, there may have been some inaccuracy in determining the peak widths because of their weak intensity and the significant background from the silicon nitride window. The second reason is more interesting as it alludes to the structure of the PBAs: while the three-dimensional structure shown in Fig. 1.1 has bonds stabilizing it along the vertical axis, these forces are absent in the proposed two-dimensional structure, allowing for out-of-plane buckling and bending. This distorts the perfect crystalline structure, leading to the high strain.

The positions of the diffraction rings also allude to the atomic structure of the PBA nanocrystals. Traditional three-dimensional PBA, formed with a hexacyanide group, forms a face-centered cubic (FCC) pattern with a unit cell size parameter around 10 Å[29]. Considering the coordination number restriction outlined in Section 1.3, two-dimensional PBA is anticipated to have a similar square crystal structure. To investigate this further, the software McMaille[54] was used to index the data. McMaille is a very powerful program that fits the measured intensities with a Le Bail fit (applying three iterations of the Rietveld decomposition formula) and uses a combination of Monte Carlo and a systematic grid search to find the underlying symmetry group and lattice structure. However, McMaille, like all available indexing software, inherently assumes that the crystal belongs to the group of three-dimensional Bravais lattices. This proves to be a bit of a problem for the two-dimensional PBA presented in this thesis; since none of the software suites consider two-dimensional crystals to be viable structures, the results of such a program must be interpreted with discretion. This is more clear upon inspection of the results of McMaille:

Based on several figures of merit, the suggested crystal structure was a primitive (P) tetragonal Bravais lattice. A tetragonal lattice is characterized by having three right-angles; that is, $\alpha = \beta = \gamma = 90^o$. Additionally, the lateral unit cell parameters $a$ and $b$ are identical, but differ from the longitudinal height $c$. This is a promising result that fits with the anticipated two-dimensional nature of the PBAs, as it can be interpreted as stacks of square crystalline monolayers. The best fit unit cell parameters were $a = b = 4.0159$ Å and $c = 15.8239$ Å. The in-plane dimensions are significantly smaller than the $\approx 10$ Å that is expected based on the three-dimensional PBA structure (see Fig. 1.1). While this could reflect the true dimensions of the two-dimensional unit cell, it is likely an artifact of the inherent three-dimensional nature of the indexing software. However, the recovered aspect ratio fits well with the proposed model of stacks of PBA monolayers.

While the previous results concerned polycrystalline ring patterns, further measurements were performed to glean information on the crystal structure of the two-dimensional PBA.

Using the smallest diffraction aperture available, selected area diffraction patterns were recorded from individual nanocrystals. Several representative patterns are shown in Fig. 4.4. Even though the diffraction aperture selected an area of only a few square micrometers, some of the diffraction patterns still showed slightly polycrystalline character. For instance, Fig. 4.4 C shows a diffraction pattern resulting from two single crystals. However, some of the patterns, such as Fig. 4.4 A, clearly show single-crystal character. These measurements suggest that each of the flakes observed in the bright-field images (see Chapter 5) are single-crystals of two-dimensional PBA.

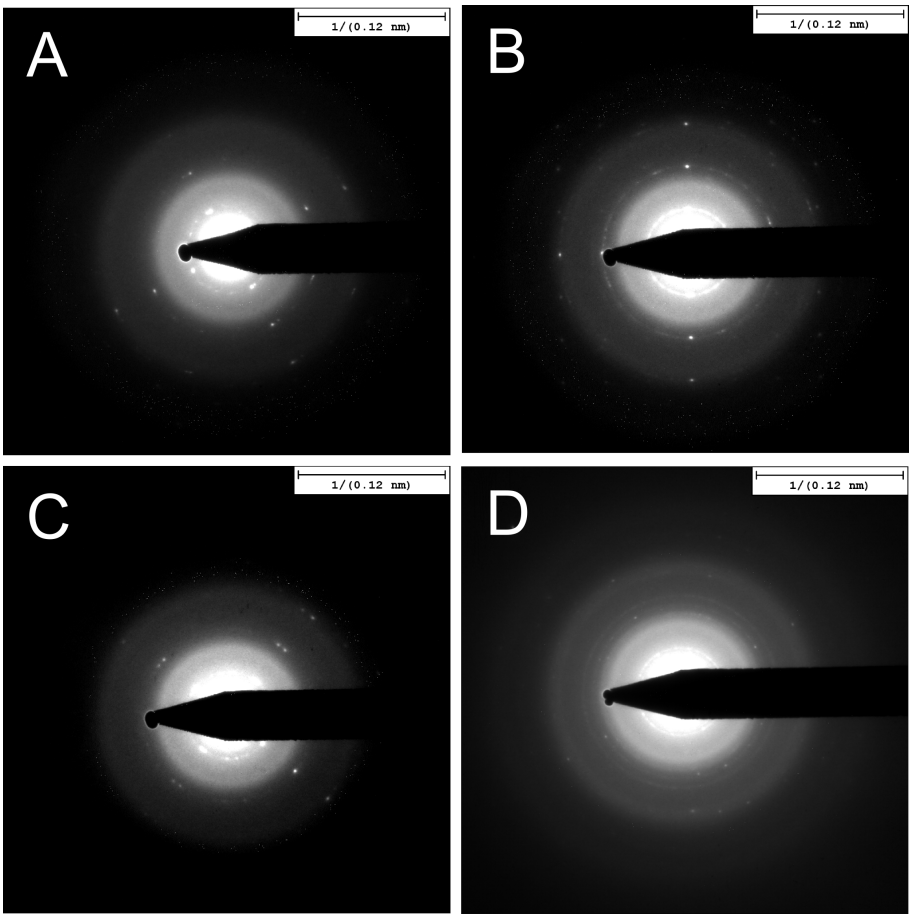


Figure 4.4: Representative selected area diffraction patterns showing the single-crystal nature of the two-dimensional Prussian blue analogue flakes.

# 5 Results: Bright-Field Imaging

As mentioned in Section 2.2, bright-field TEM images provide information relating to the film morphology, domain sizes, and other important structural characteristics. This chapter discusses the results of bright-field images of the two-dimensional PBA films.

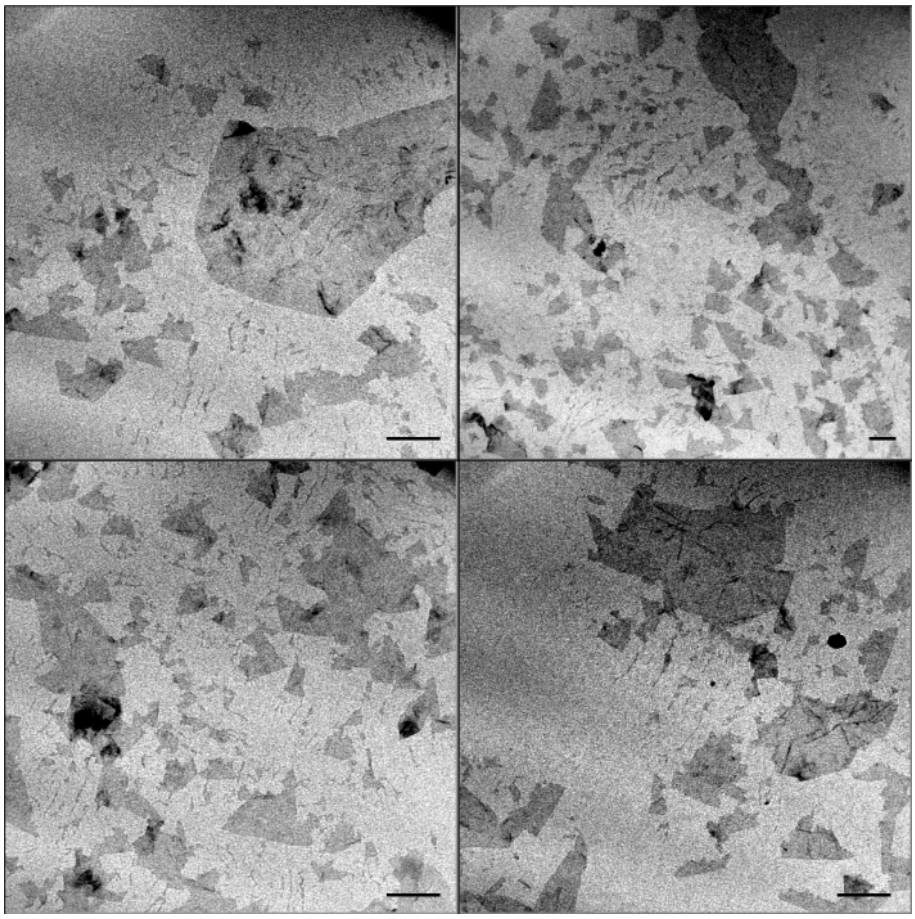

Figure 5.1: Representative bright-field images of Prussian blue analogues on a thin silicon nitride membrane taken with a transmission electron microscope. The scale bar in each image represents 500 nm.

Fig. 5.1 shows several representative high magnification TEM micrographs of the two-dimensional PBA deposited on a silicon nitride window. Many flakes are visible with varying sizes and apparent thicknesses. Based on the control experiments mentioned

in Chapter 3 and the diffraction data in Chapter 4, we can conclude that these flakes correspond to nanocrystals of PBA. The distribution of the nanocrystal areas is shown in Fig. 5.2. Although heavily weighted towards smaller crystals, the distribution reveals that a significant fraction (over 15 %) of the crystals were quite large (over 10,000 $nm^2$ in area). The average area was around 6,500 $nm^2$, while the median was around 2,100 $nm^2$. These roughly correspond to lateral sizes just over 80 nm and 45 nm, respectively, if the nanocrystals are considered to be approximately square. These values can be compared with the size determined from the diffraction data shown in Chapter 4, where it was found that the coherence length of the crystalline domains was $\approx$ 10 nm. This is smaller than the values determined by the bright-field images, but, as discussed in Chapter 4, this is likely due to inaccuracy in determining the diffraction peak widths. The sizes determined from the bright-field images are consisten with what has been measured in three-dimensional PBAs[53].

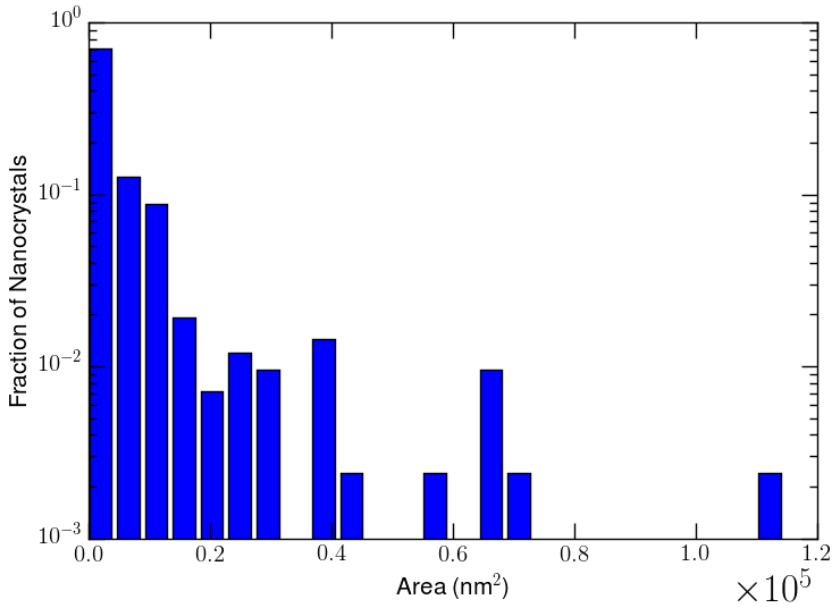


Figure 5.2: Distribution of PBA nanocrystal areas as determined from bright-field TEM images.

To characterize the thicknesses of the nanocrystals, it should be noted that all bright-field images showed relatively low contrast; for instance, the difference in the image intensity between the bare substrate and the substrate containing PBA was only around 20 % (see Fig. 5.4 A). This result suggests that the PBA nanocrystals are very thin. In addition, some flakes are significantly darker or lighter than others, indicative of a variation in flake thickness. Because the mechanism behind bright-field imaging is amplitude (diffraction) contrast, as presented in Section 2.2, this discussion can be quantified by comparing the intensity of the bright-field image of the bare substrate with that of the PBA film. In the

absence of PBA, the intensity in the bright-field image is given by

$$I_{sub} = I_0 \exp\left(-\mu_{sub} t_{sub}\right) \tag{5.1}$$

where $I_0$ is the incident electron beam intensity, and $\mu_{sub}$ and $t_{sub}$ are the substrate's attenuation coefficient and thickness, respectively (see Eq.(2.3) and Section 2.2 for thorough discussion of these parameters). To account for the presence of PBA, this expression is modified to

$$I_{PBA} = I_0 \exp\left(-\mu_{sub} t_{sub} - \mu_{PBA} t_{PBA}\right) \tag{5.2}$$

where the variables are similarly defined. These expressions can be combined in terms of the ratio of the intensity of the two images as

$$\frac{I_{PBA}}{I_{sub}} = \exp\left(-\mu_{PBA} t_{PBA}\right) \tag{5.3}$$

Thus using the measured intensities of the bright-field images of PBA on the silicon nitride substrate, the thickness of the PBA layer can be estimated. To do so, Eq.(2.4) is used for the linear attenuation coefficient of PBA:

$$\mu_{PBA} = \sum_i \sigma_i^{tot}(\beta) N_i \tag{5.4}$$

where the sum runs over the distinct atoms in PBA, i.e. $i$ =C, N, Pt, Cu.

Computing the number of $i$ atoms per unit volume, $N_i$, requires some assumptions about the structure of PBA. The arguments based on coordination number restriction presented in Section 1.3 conclude that PBA forms two-dimensional crystals, and the diffraction data in Chapter 4 suggests that the crystals are square. If we make the assumption that the PBA unit cell is square with a side length $a$ and thickness $L_{PBA}$, then

$$N_i = \frac{n_i}{a^2 L_{PBA}} \tag{5.5}$$

where $n_i$ is the number of $i$ atoms in the unit cell.

With this treatment of the PBA structure as true monolayers, the flakes shown in Fig. 5.1 can be thought of as stacks of $m$ PBA monolayers resulting in a total thickness

$t_{PBA} = mL_{PBA}$. This model is supported by the results of the indexing of the diffraction data, which suggested that the two-dimensional PBA crystals were tetragonal, with a square base but a large aspect ratio in the vertical direction. Therefore, the contrast with the substrate given in Eq.(5.3) becomes

$$\frac{I_{PBA}}{I_{sub}} = \exp\left[-\frac{m}{a^2}\sum_i n_i \sigma_i^{tot}(\beta)\right] \tag{5.6}$$

By using an estimate for the unit cell size $a$, this equation can be inverted to calculate the number of monolayers $m$ of each flake:

$$m = \frac{a^2}{2\sigma_{Pt}^{tot}(\beta) + 2\sigma_{Cu}^{tot}(\beta) + 8\sigma_C^{tot}(\beta) + 8\sigma_N^{tot}(\beta)} \ln\left(\frac{I_{sub}}{I_{PBA}}\right) \tag{5.7}$$

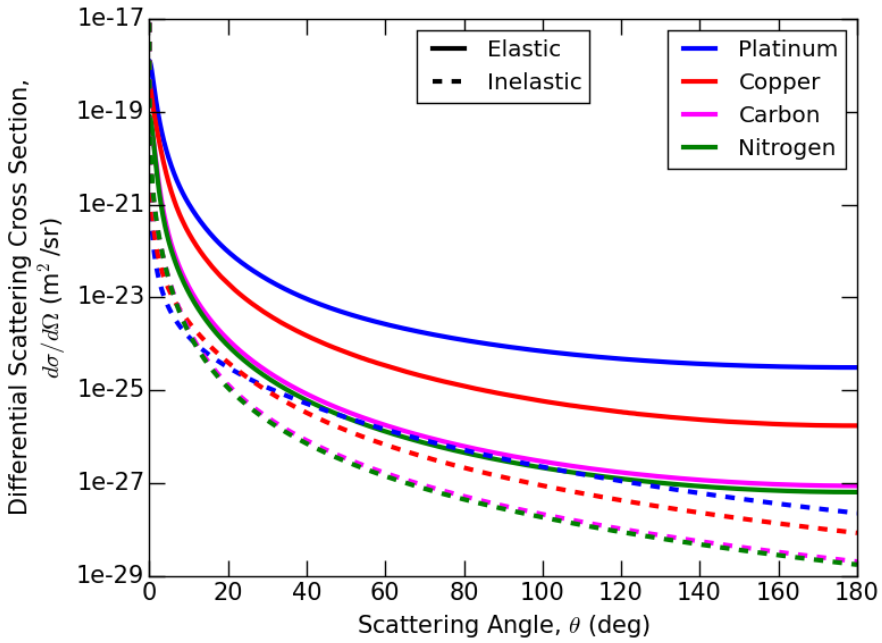


Figure 5.3: Elastic (solid lines) and inelasic (dashed lines) differential scattering cross sections for the atomic constituents of PBA: platinum (blue), copper (red), carbon (magenta), and nitrogen (green)

A good estimation of the number of monolayers thus requires a careful calculation of the total scattering cross sections. The elastic cross sections were calculated using the experimental values for the differential scattering cross sections[55]. The inelastic cross sections were calculated using the Wentzel model for the screened atomic potential[43] as:

$$\sigma_i^{inel}(\beta) = \frac{4Z_i^{1/3}\lambda^2(1+E/E_0)^2}{\pi}\left[\ln\sqrt{1+(\theta_0/\beta)^2} - \frac{1}{4\left[1+(\beta/\theta_0)^2\right]}\right] \tag{5.8}$$

where $Z_i$ is the atomic number of the $i^{th}$ element, $\lambda$ and $E$ are the electron's wavelength and kinetic energy, respectively, $E_0 = m_e c^2 = 511$ keV is an electron's rest energy, and $\theta_0 = \lambda Z_i^{1/3}/2\pi a_{\mathrm{H}}$ is the characteristic angle of the $i^{th}$ element, with $a_{\mathrm{H}} = \epsilon_0 h^2/\pi m_e q^2 = 0.0529$ nm being Bohr's radius. Fig. 5.3 shows the differential cross sections used to calculate the total cross section $\sigma_i^{tot}(\beta)$ in the following estimation of the number of monolayers, $m$.

Fig. 5.4 A shows the the contrast ratio $(I_{sub} - I_{PBA})/I_{sub}$ measured for many flakes; the distribution in these values results from the fact that the flakes have varying thicknesses. If we take $a \approx 10$ Å (as expected from the proposed structure; see Section 1.3) and use Eq.(5.7), the distribution in number of monolayers shown in Fig. 5.4 B is obtained. It is evident that the majority of the PBA flakes are very thin, with over 25 % of the observed flakes consisting of less than five monolayers, and around 20 % of the flakes being true monolayers (see Fig. 5.4 B, inset). However, the distribution is quite broad, spanning all the way to several hundreds of monolayers in thickness. Each thickness is only populated by a few percent of flakes, but in together these thick films represent about half of the observed PBA crystals. The coexistence of true monolayers and thick flakes is puzzling, especially considering that such thickness variation was observed from flakes created from the same LS film. This suggests the conclusion that the inverted LS method described in Chapter 3 does successfully produce two-dimensional monolayers of PBA, but the deposition process during transfer to the substrate leads to stacking and layering of the film. This is most likely to have occurred during the final compression prior to deposition; because the inverted LS method inherently produces solid films without the compression step of traditional LS, the film is already in its equilibrium solid state and so the force of the final compression has no option but to layer to film. Regardless of the breadth of the distribution, it is encouraging that the majority of the PBA flakes are monolayers. This is in support the expected two-dimensional nature of the films.

Finally, it should be stressed that these results are rather sensitive[1] to the choice of the unit cell size $a$. In fact, because of the quadratic dependence in Eq.(5.7), a 1 % change in $a$ results in a 2 % change in the number of monolayers $m$. Therefore, because the value of $a = 10$ Å was arrived at indirectly, there remains some uncertainty in these results in terms of $m$.

[1]This is quantified by defining the *sensitivity* $S(x)$, which is the percent change in the output a model $f(x)$ to a 1% change in the model parameter $x$, as $S(x) = xf'(x)/f(x)$

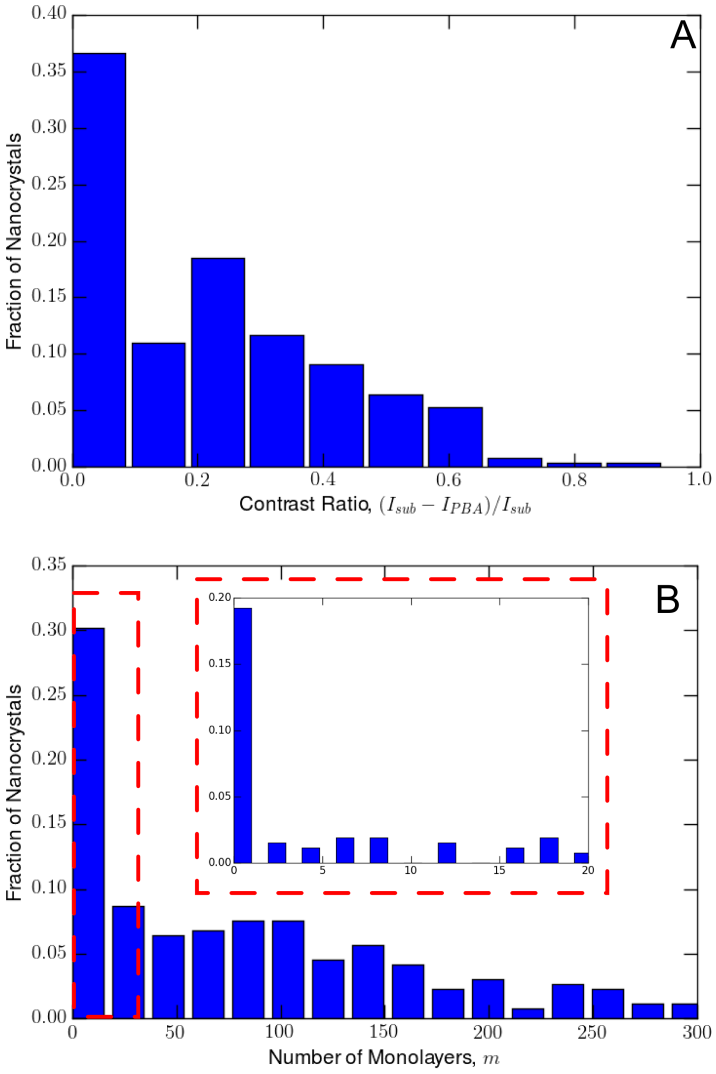


Figure 5.4: (A) Distribution of contrast ratio observed in bright-field TEM images of PBA. (B) Corresponding distribution of flake thicknesses in terms of number of PBA monolayers.

# 6 Conclusions

This thesis bridges the gap between two exciting fields of contemporary materials science research: two-dimensional systems and functional coordination compounds. The former is, of course, a booming field, and in the last decade or so an immense amount of progress has been made in producing monolayer materials beyond graphene. The goal is to make these two-dimensional materials useful; that is where the latter field of coordination compounds comes into play. Prussian Blue Analogues (PBAs) are a particularly exciting candidate, due to the plethora of uses they have found in various applications. To this end, this thesis presented a proof-of-principle experiment in which the production of two-dimensional crystals of PBA was successfully demonstrated.

Quantifying the quality of the two-dimensional PBA nanocrystals was performed by extensive transmission electron microscopy (TEM) measurements. This is a powerful technique that provides nanoscopic details on the morphology and topology of thin samples and crystals. Measurements were performed in both bright-field imaging and selected area diffraction modes. These modes were chosen because they provide information on a variety of structural parameters; for instance, the nanocrystallite size, strain, and thickness. Combined, these form a complete picture of the two-dimensional nature of the PBA films.

To achieve the reduction in dimensionality from the traditional three-dimensional cubic PBA structure to the proposed two-dimensional monolayers, coordination number restriction on the cyanide groups was imposed: by substituting the conventional hexacyanide group with a tetracyanide, the PBA was expected to form an inherently planar structure, as introduced in Chapter 1. When created using a novel variant on the Langmuir-Schaefer (LS) method, the PBA films were observed to contain small domains of single-crystals. This was confirmed by selected area electron diffraction, which additionally shed light on the crystallinity of each nanocrystal. Strain was observed at slightly higher levels than what is typical in three-dimensional PBA crystals. This is likely due to out-of-plane buckling in the flexible cyanide bridges, a freedom that is only present due to the planar structure. The diffraction patterns also hint at a two-dimensional square structure, in

support of the proposed structural model.

Real-space images in bright-field mode confirmed the nanocrystallite domain size measured from the diffraction patterns. Additionally, the thickness of the PBA films were estimated by using the contrast between the substrate and the PBA films. This made use of an appropriate estimate of the Pt-Pt bond distance, and it was found that almost 20 % of the observed crystals were true monolayers. Thicker crystals were interpreted to be stacks of monolayers, and were likely to have formed during the deposition of the LS films onto the substrate.

The TEM data presented in this thesis supports the conclusion that crystalline monolayers of two-dimensional monolayers of PBA were successfully synthesized. This constitutes a proof-of-principle experiment that shows that it is possible to produce two-dimensional PBA via an interfacial reaction and the LS technique.

# Bibliography


[1] D. R. Smith, W. J. Padilla, D. C. Vier, S. C. Nemat-Nasser, and S. Schultz, "Composite medium with simultaneously negative permeability and permittivity," *Physical Review Letters*, vol. 84, p. 4184, 2000.

[2] R. Mankowsky, A. Subedi, M. Först, S. Mariager, M. Chollet, H. T. Lemke, J. S. Robinson, J. M. Glownia, M. P. Minitti, A. Frano, M. Fechner, N. A. Spaldin, T. Loew, B. Keimer, G. A., and C. A., "Nonlinear lattice dynamics as a basis for enhanced superconductivity in $YBa_2Cu_3O_{6.5}$," *Nature*, vol. 516, pp. 71–73, 2014.

[3] K. K. Gomes, W. Mar, W. Ko, F. Guinea, and H. C. Manoharan, "Designer Dirac fermions and topological phases in molecular graphene," *Nature*, vol. 483, pp. 306–310, 2012.

[4] S. Z. Butler, S. M. Hollen, L. Cao, Y. Cui, J. A. Gupta, H. R. Gutiérrez, T. F. Heinz, S. S. Hong, J. Huang, A. F. Ismach, E. Johnston-Halperin, M. Kuno, V. V. Plashnitsa, R. D. Robinson, R. S. Ruoff, S. Salahuddin, J. Shan, L. Shi, M. G. Spencer, M. Terrones, W. Windl, and J. E. Goldberger, "Progress, challenges, and opportunities in two-dimensional materials beyond graphene," *ACS Nano*, vol. 7, pp. 2898–2926, 2013.

[5] P. Miró, M. Audiffreda, and T. Heine, "An atlas of two-dimensional materials," *Chemical Society Reviews*, vol. 43, pp. 6537–6554, 2014.

[6] S. SidongLei, F. Wen, B. Li, Q. Wang, Y. Huang, Y. Gong, Y. He, P. Dong, J. Bellah, A. George, L. Ge, J. Lou, N. J. Halas, R. Vajtai, and P. M. Ajayan, "Progress, challenges, and opportunities in two-dimensional materials beyond graphene," *Nano Letters*, vol. 15, pp. 259–265, 2015.

[7] X. Sun, Z. Liu, K. Welsher, J. T. Robinson, A. Goodwin, S. Zaric, and H. Dai,

"Nano-graphene oxide for cellular imaging and drug delivery," *Nano Research*, vol. 1, pp. 203–212, 2008.

[8] A. A. Karyakin, "Prussian blue and its analogues: Electrochemistry and analytical applications," *Electroanalysis*, vol. 13, pp. 813–819, 2001.

[9] F. Ricci and G. Palleschi, "Sensor and biosensor preparation, optimisation and applications of Prussian blue modified electrodes," *Biosensors and Bioelectronics*, vol. 21, pp. 389–407, 2005.

[10] D. Yang, J. Xu, X.-Z. Liao, Y.-S. He, H. Liub, and Z.-F. Ma, "Structure optimization of Prussian blue analogue cathode materials for advanced sodium ion batteries," *Chemical Communications*, vol. 50, pp. 13377–13380, 2014.

[11] N. R. de Tacconi, K. Rajeshwar, and R. O. Lezna, "Metal hexacyanoferrates: Electrosynthesis, in situ characterization, and applications," *Chem. Mater.*, vol. 15, pp. 3046–3062, 2003.

[12] S. Ferlay, T. Mallah, O. R., P. Veillet, and M. Verdaguer, "A room-temperature organometallic magnet based on Prussian blue," *Nature*, vol. 378, pp. 701–703, 1995.

[13] J. M. Manriquez, G. T. Yee, R. S. McClean, A. J. Epstein, and J. S. Miller, "A room-temperature molecular/organic-based magnet," *Science*, vol. 252, pp. 1415–1417, 1991.

[14] O. Sato, T. Iyoda, A. Fujishima, and K. Hashimoto, "Photoinduced magnetization of a cobalt-iron cyanide," *Science*, vol. 272, pp. 704–705, 1996.

[15] S.-I. Ohkoshi, S. Yorozu, O. Sato, T. Iyoda, A. Fujishima, and K. Hashimoto, "Photoinduced magnetic pole inversion in a ferro-ferrimagnet: $(Fe^{II}_{0.40}Mn^{II}_{0.60})_{1.5}Cr^{III}(CN)_6$," *Applied Physics Letters*, vol. 70, p. 1040, 1997.

[16] S.-I. Ohkoshi, T. Iyoda, A. Fujishima, and K. Hashimoto, "Magnetic properties of mixed ferro-ferrimagnets composed of Prussian blue analogs," *Physical Review B*, vol. 56, p. 11642, 1997.

[17] S.-I. Ohkoshi, Y. Abe, A. Fujishima, and K. Hashimoto, "Design and preparation of a novel magnet exhibiting two compensation temperatures based on molecular field theory," *Physical Review Letters*, vol. 82, p. 1285, 1999.

[18] W. Kosaka, M. Tozawa, K. Hashimoto, and S.-I. Ohkoshi, "Synthesis and superparamagnetic property of a CoCr prussian blue analogue nanoparticles inside Nafion membrane," *Inorganic Chemistry Communications*, vol. 9, pp. 920–922, 2006.

[19] L. Catala, A. Gloter, O. Stephan, G. Rogez, and T. Mallah, "Superparamagnetic bimetallic cyanide-bridged coordination nanoparticles with $T_b$ = 9 K," *Chemical Communications*, vol. 9, pp. 1018–1020, 2006.

[20] W. E. Buschmann, J. Ensling, P. Gütlich, and J. S. Mille, "Electron transfer, linkage isomerization, bulk magnetic order, and spin-glass behavior in the iron hexacyanomanganate Prussian blue analogue," *Chemistry: A European Journal*, vol. 5, pp. 3019–3028, 1999.

[21] E. Coronado, M. C. Giménez-López, T. Korzeniak, G. Levchenko, F. M. Romero, A. Segura, V. García-Baonza, J. C. Cezar, F. M. F. de Groot, A. Milner, and M. Paz-Pasternak, "Pressure-induced magnetic switching and linkage isomerism in $K_{0.4}Fe_4[Cr(CN)_6]_{2.8}\cdot 16H_2O$: X-ray -absorption and magnetic circular dichroism studies," *Journal of the American Chemical Society*, vol. 130, pp. 15519–15532, 2008.

[22] S. Margadonna, K. Prassides, and A. N. Fitch, "Zero thermal expansion in a Prussian blue analogue," *Journal of the American Chemical Society*, vol. 126, pp. 15390–15391, 2004.

[23] K. W. Chapman, P. J. Chupas, and C. J. Kepert, "Compositional dependence of negative thermal expansion in the Prussian blue analogues $M^{II}Pt^{IV}(CN)_6$ (M = Mn, Fe, Co, Ni, Cu, Zn, Cd)," *Journal of the American Chemical Society*, vol. 128, pp. 7009–7014, 2006.

[24] A. L. Goodwin, K. W. Chapman, and C. J. Kepert, "Guest-dependent negative thermal expansion in nanoporous Prussian blue analogues $M^{II}Pt^{IV}(CN)_6 \cdot x\{H_2O\}$ ($0 \leq x \leq 2$; M = Zn, Cd)," *Journal of the American Chemical Society*, vol. 127, pp. 17980–17981, 2005.

[25] S. Kaye and J. Long, "Hydrogen storage in the dehydrated prussian blue analogues $M_3[Co(CN)_6]_2$ (M = Mn, Fe, Co, Ni, Cu, Zn)," *Journal of the American Chemical Society*, vol. 127, pp. 6506–6507, 2005.

[26] R. J. Mortimer, "Electrochromic materials," *Chemical Society Reviews*, vol. 3, pp. 147–156, 1997.

[27] P. J. Kulesza, K. Miecznikowski, M. Chojak, M. A. Malik, S. Zamponi, and R. Marassi, "Electrochromic features of hybrid films composed of polyaniline and metal hexacyanoferrate," *Electrochimica Acta*, vol. 46, pp. 4371–4378, 2001.

[28] M. Kaneko, S. Hara, and A. J. Yamada, "A photoresponsive graphite electrode coated with Prussian blue," *Journal of Electroanalytical Chemistry and Interfacial Electrochemistry*, vol. 194, pp. 165–168, 1985.

[29] A. Ludi and H. U. Güdel, "Structural chemistry of polynuclear transition metal cyanides," *Structure and Bonding*, vol. 14, pp. 1–21, 1973.

[30] M. P. Shores, L. G. Beauvais, and J. R. Long, "Cluster-expanded Prussian blue analogues," *Journal of the American Chemical Society*, vol. 121, pp. 775–779, 1999.

[31] K. Itaya, T. Ataka, and S. Toshima, "Spectroelectrochemistry and electrochemical preparation method of Prussian blue modified electrodes," *Journal of the American Chemical Society*, vol. 104, pp. 4767–4772, 1982.

[32] C. A. Lundgren and R. W. Murray, "Observations on the composition of Prussian blue films and their electrochemistry," *Inorganic Chemistry*, vol. 27, pp. 933–939, 1988.

[33] V. D. Neff, "Some performance characteristics of a Prussian blue battery," *Journal of the Electrochemical Society*, vol. 132, pp. 1382–1384, 1985.

[34] R. J. Mortimer and D. R. Rosseinsky, "Electrochemical polychromicity in iron hexacyanoferrate films, and a new film form of ferric ferricyanide," *Journal of Electroanalytical Chemistry and Interfacial Electrochemistry*, vol. 151, pp. 133–147, 1983.

[35] N. Toshima, R.-J. Lin, and M. Kaneko, "Electrochemical polychromicity in iron hexacyanoferrate films, and a new film form of ferric ferricyanide," *Journal of Electroanalytical Chemistry and Interfacial Electrochemistry*, vol. 19, pp. 485–488, 1990.

[36] V. D. Neff, "Electrochemical oxidation and reduction of thin films of Prussian blue," *Journal of the Electrochemical Society*, vol. 125, pp. 886–887, 1978.

[37] R. Y. N. Gengler, L. M. Toma, E. Pardo, F. Lloret, X. Ke, G. Van Tendeloo, D. Gournis, and P. Rudolf, "Prussian blue analogues of reduced dimensionality," *Small*, vol. 8, pp. 2532–2540, 2012.

[38] Y. Umemura, "Hybrid films of a clay mineral and an iron(II) complex cation prepared by a combined method of the Langmuir-Blodgett and self-assembly techniques," *Journal of Physical Chemistry B*, vol. 106, pp. 11168–11171, 2002.

[39] C. Mühle, J. Nuss, and M. Jansen, "Crystal structure of tetracyanoplatinate(IV) dihydrate, $Pt(CN)_4 \cdot H_2O$," *Z. Kristallogr. NCS*, vol. 224, pp. 9–10, 2009.

[40] S. Roth and D. Carroll, *One-Dimensional Metals, 2nd Edition*. Weinheim: Wiley-VCH, 2009.

[41] D. S. Badali, A. Rossos, R. Y. N. Gengler, and R. J. D. Miller, "Synthesis of atomically thin Prussian blue analogue films using an inverted Langmuir-Schaefer method." in preparation, 2015.

[42] D. B. Williams and C. B. Carter, *Transmission Electron Microscopy: A Textbook for Materials Science*. Berlin: Springer, 2009.

[43] L. Reimer and H. Kohl, *Transmission Electron Microscopy: Physics of Image Formation, 5th Edition*. Berlin: Springer, 2008.

[44] P. Scherrer, "Bestimmung des Grösse und der inneren Struktur von Kolloidteilchen mittels Röntgenstrahlen," *Nachr. Ges. Wiss. Göttingen*, vol. 26, pp. 98–100, 1918.

[45] A. R. Stokes and A. J. C. Wilson, "The diffraction of X rays by distorted crystal aggregates - I," *Proc. Phys. Soc. Lond.*, vol. 56, pp. 174–181, 1944.

[46] G. K. Williamson and W. H. Hall, "X-ray line broadening from filed aluminium and wolfram," *Acta Metallurgica*, vol. 1, pp. 22–31, 1953.

[47] A. Rossos, *Development and study of novel nano-structured hybrid materials based on carbon*. PhD thesis, University of Ioannina, 2014.

[48] E. J. Sonneveld and J. W. Visser, "Automatic collection of powder data from photographs," *Journal of Applied Crystallography*, vol. 8, pp. 1–7, 1975.

[49] X. Li, A. Mighell, and V. L. Karen, "NIST Metals Structural Database, NIST Standard Reference Database 83," tech. rep., National Institute of Standards and Technology, Gaithersburg, Maryland, 20899-8320, 2008.

[50] A. Maeland and T. B. Flanagan, "Lattice spacings of gold-palladium alloys," *Canadian Journal of Physics*, vol. 42, pp. 2364–2366, 1964.

[51] P. Bhatt, S. Banerjee, S. Anwar, S. Mukadam, Mayuresh D. Singh Meena, and S. M. Yusuf, "Core-shell Prussian blue analogue molecular magnet $Mn_1.5[Cr(CN)_6]\cdot mH_2O@Ni_{1.5}[Cr(CN)_6]\cdot nH_2O$ for hydrogen storage," *ACS Applied Materials and Interfaces*, vol. 130, pp. 17579–17588, 2008.

[52] V. Trannoy, E. Delahaye, G. Fornasieri, P. Beaunier, and A. Bleuzen, "Using Prussian blue analogue nanoparticles confined into ordered mesoporous silica monoliths as precursors of oxides," *Comptes Rendus Chimie*, vol. 17, pp. 512–520, 2014.

[53] L. Samain, F. Grandjean, G. J. Long, P. Martinetto, P. Bordet, and D. Strivay, "Relationship between the synthesis of Prussian blue pigments, their color, physical properties, and their behavior in paint layers," *Journal of Physical Chemistry C*, vol. 117, pp. 9693–9712, 2013.

[54] A. Le Bail, "Monte Carlo indexing with McMaille," *Powder Diffraction*, vol. 19, pp. 249–254, 2004.

[55] A. Jablonski, F. Salvat, and C. J. Powell, "NIST Electron Elastic-Scattering Cross-Section Database - Version 3.2," tech. rep., National Institute of Standards and Technology, Gaithersburg, Maryland, 20899-8320, 2010.